AIAA SciTech Forum
9 - 13 January 2017, Grapevine, Texas
AIAA Guidance, Navigation, and Control Conference

CrossMark
click for updates

Experimental Validation for Tethered Capture of Spinning Space Debris

Kirk Hovell* and Steve Ulrich†
Carleton University, Ottawa, ON, K1S 5B6, Canada

The space debris population has been growing steadily since Sputnik was launched in 1957. Recently, the risk of cascaded collisions between debris has become a concern, as this has the ability to render certain popular orbits too risky to continue using. Debris mitigation is important to limit the growth of the debris population, but active debris removal has been found to be necessary to keep the current debris quantity from growing. An active debris removal mission consists of a chaser spacecraft performing a rendezvous with a target object, capturing it, and towing it to a disposal orbit or into the atmosphere. Capturing the debris has challenges because of residual angular momentum present in the uncooperative debris. This paper examines techniques for dissipating the angular momentum present in a target debris using visco-elastic tethers, through numerical simulations and planar experiments in the Spacecraft Robotics and Control Laboratory at Carleton University. Both simulation and experimental results agree that a tether configuration with multiple tether attachment points on a target is significantly faster at stabilizing a spinning debris than the currently accepted single tether configuration.

Nomenclature

$\mathbf{A}$	Attitude matrix
$\vec{\mathcal{F}}_x$	Vectrix of reference frame x
τ	Torque, N·m
F	Force, N
m	Mass, kg
J	Moment of inertia, kg·m^2
L	Length, m
$\mathbf{a}_x$	Tether attachment point to body x with respect to x's centre of mass, m
θ	Angle, deg
ω	Angular rate, deg/s
$\mathbf{r}$	Position vector components, m
$\mathbf{v}$	Velocity vector components, m/s
k	Stiffness, N/m
c	Damping coefficient, N·s/m
$\mathbf{K}_P$	Proportional gain matrix
$\mathbf{K}_D$	Derivative gain matrix
$\mathbf{I}_{x\times x}$	Identity matrix of dimension x
$\dot{x}$	Time derivative of x
$\ddot{x}$	Second time derivative of x
$\vec{x}$	Physical vector x
$\|\mathbf{x}\|$	Euclidean norm of $\mathbf{x}$
$\mathbf{x}$	Three dimensional components of physical vector $\vec{x}$

*Graduate Student, Department of Mechanical and Aerospace Engineering, 1125 Colonel By Drive. Student Member AIAA.
†Assistant Professor, Department of Mechanical and Aerospace Engineering, 1125 Colonel By Drive. Senior Member AIAA.

Copyright © 2017 by Kirk Hovell and Steve Ulrich. Published by the American Institute of Aeronautics and Astronautics, Inc., with permission.

Downloaded by CARLETON UNIVERSITY on January 24, 2017 | http://arc.aiaa.org | DOI: 10.2514/6.2017-1049

Subscript

I	Inertial reference frame
t, j, c	Refers to target, junction, and chaser, respectively

Superscript

T	Transpose
t	Target body-fixed frame
c	Chaser body-fixed frame
$\times$	Skew-symmetric matrix

I. Introduction

In early 2015, there were more than 17,000 objects larger than 10 cm in orbit around the Earth, but only 23% of them were operational spacecraft.[1] The defunct spacecraft that remain in orbit are named *space debris*. Leaving non-operational spacecraft in orbit was not thought of as a problem until 1978 when Kessler studied the collision frequency of spacecraft and found that while the density of spacecraft in low Earth orbit orbit is small, the collision frequency is non-zero and the debris population has exponential growth.[2] This phenomenon was later called the *Kessler Syndrome*, which describes how collisions between spacecraft significantly increase the number of space debris, further increasing the chance of a collision. More recent studies by the European Space Agency have revealed that 5 to 10 properly selected pieces of space debris must be actively removed per year for the current number of space debris to remain stable.[3]

Reports have outlined various techniques and associated challenges for actively removing space debris.[1,3,4] Most techniques involve a chaser spacecraft that performs a rendezvous with the target debris. After rendezvous, either a rigid or flexible connection is made with the debris. This connection is used to stabilize the likely spinning debris,[4] and then tow or push the debris into a lower orbit where it is released to decay into the atmosphere. Rigid connections often use a mechanical arm[5] or a grapple.[6] Difficulties with rigid connections occur when the debris has angular rates about all three axes. However, due to energy dissipation and the major axis rule, eventually all debris will have a single axis spin.[4] For this reason, a significant amount of research is being performed on using robotic manipulators to capture debris.[5–7] Along with rigid connections between the chaser and target, flexible connections are also possible.

There are three main techniques for deorbiting debris using flexible connections. First, a harpoon can be used to establish a tethered connection between the chaser and the debris. This method involves launching a harpoon from the chaser that penetrates the multi-layer insulation of the target and becomes embedded in the target.[8] A flexible tether attaches the harpoon to the chaser. Once the harpoon is embedded in the target, the chaser can then use its thrusters to tow the target to its disposal orbit. Electrodynamic tethers are another approach that are purely passive once initiated. A chaser attaches a multi-kilometer conductive tether to the target debris, that hangs in the nadir direction. The electrodynamic tether captures and conducts ions through its length. This current produces an electromagnetic field around the tether that interacts with the Earth's magnetic field, producing a deorbiting thrust.[9–11] The chaser is not connected to the electrodynamic tether, so it is free to pursue other debris once it attaches the tether to the target. The third, and perhaps most universal capture technique, is to use a net and tether. A net is launched from a chaser spacecraft and envelops a target. A tether is attached to both the net and the chaser such that the chaser can use its thrusters to have some control over the tumbling target. Advantages to the net and tether technique are that it does not require a specific attachment point on the target, it can capture various sizes of targets, and the targets can have angular rates about all three axes. Net capturing research is highly active at present. Simulations[12–15] and experiments[16–18] have been performed to understand how a net wraps around a target and how it remains secured. This paper does not consider how the Tethered Spacecraft System (TSS) was established, but assumes that a tethered connection between the chaser and target was created either using a net or harpoon. Other researchers have taken the same approach to investigate the control aspects of towing a debris out of orbit using a TSS.[19–21] The towing phase of the mission begins after the target has been both securely captured and stabilized. The transient portion of the debris capture mission between when the net or harpoon attaches to the target and when the towing phase begins, i.e., the target stabilization phase, is often neglected.

This paper examines the target stabilization phase. Specifically, this work investigates the stabilization of a tumbling target with vicso-elastic tethers. It assumes that a net or harpoon has already been deployed such that the chaser and target are tethered together and the target is spinning. While some in-depth

Downloaded by CARLETON UNIVERSITY on January 24, 2017 | http://arc.aiaa.org | DOI: 10.2514/6.2017-1049

simulations of TSS dynamics have been recently presented,[22–24] this paper specifically examines the effect of different tether configurations on the stabilization ability of the TSS. This paper builds on previous on-orbit simulations[25] by presenting further numerical simulations along with experimental validation. Two different tether configurations are presented. The first configuration uses a single tether that attaches the chaser to the target. The second, novel, configuration has a single tether attached to the chaser that splits into two sub-tethers that are attached at various locations on the target. In this paper, results of numerical simulations are presented and compared to planar experiments in Carleton University's Spacecraft Robotics and Control Laboratory.

Section II presents the two-dimensional equations of motion for a TSS. Section III presents numerical simulations for each tether configuration and discusses the results. Section IV discusses the experimental setup, presents experimental results, and compares the results of the experiments to those of the simulations. Section V draws conclusions on the work presented, and summarizes the contributions of this paper.

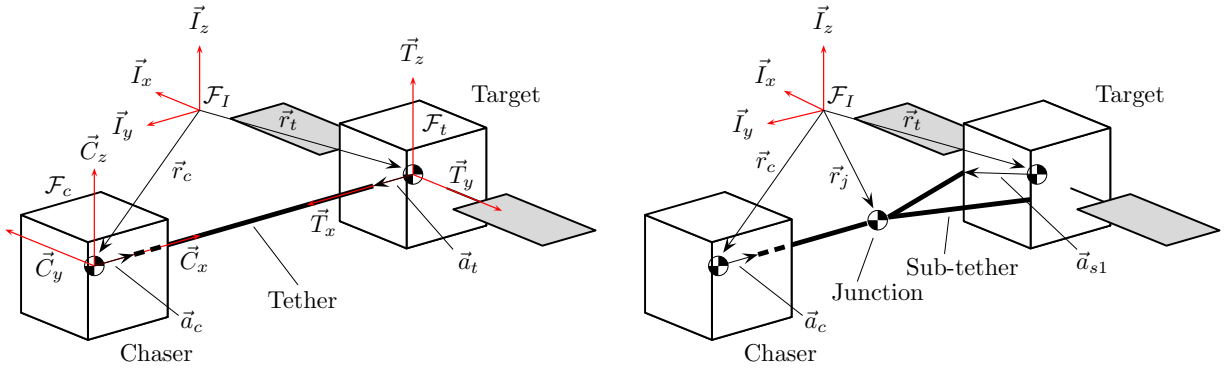

(a) Single tether configuration with reference frame definition.

(b) Sub-tether configuration. For clarity, $\mathcal{F}_c$, $\mathcal{F}_t$, and $\vec{a}_{s2}$ are omitted.

Figure 1. Reference frame and vector definition for planar dynamics modeling.

II. Planar Dynamics Formulation

Referring to Fig. 1, $\mathcal{F}_I$ represents the inertial reference frame, and vector $\vec{r}_t$ represents the position vector of the centre of mass of the target with respect to the origin of $\mathcal{F}_I$. The vector $\vec{r}_t$ has two-dimensional components, $\mathbf{r}_t$, in the inertial frame such that

$$\vec{r}_t = \vec{\mathcal{F}}_I^{\mathrm{T}} \mathbf{r}_t. \tag{1}$$

Similarly, the two-dimensional positions of the centre of mass of the chaser and the junction are defined, respectively, as:

$$\vec{r}_c = \vec{\mathcal{F}}_I^{\mathrm{T}} \mathbf{r}_c \tag{2}$$

$$\vec{r}_j = \vec{\mathcal{F}}_I^{\mathrm{T}} \mathbf{r}_j. \tag{3}$$

In the single tether configuration in Fig. 1a, $\vec{a}_t$ denotes the two-dimensional attachment point vector of the single tether to the target, with respect to the target's centre of mass. Its components in the target body-fixed frame, $\mathcal{F}_t$, are given by:

$$\mathbf{a}_t \equiv \begin{bmatrix} a_{t,x} \\ a_{t,y} \end{bmatrix} = \vec{\mathcal{F}}_t \cdot \vec{a}_t \tag{4}$$

where $\mathbf{a}_t$ represents the two-dimensional components of the vector $\vec{a}_t$ in $\mathcal{F}_t$. Similarly, the tether attachment point vector components in the chaser body-fixed reference frame, $\mathcal{F}_c$, are given by:

$$\mathbf{a}_c \equiv \begin{bmatrix} a_{c,x} \\ a_{c,y} \end{bmatrix} = \vec{\mathcal{F}}_c \cdot \vec{a}_c \tag{5}$$

Downloaded by CARLETON UNIVERSITY on January 24, 2017 | http://arc.aiaa.org | DOI: 10.2514/6.2017-1049

where $\vec{a}_c$ is the tether attachment point vector on the chaser with respect to the chaser's centre of mass. In the sub-tether configuration shown in Fig. 1b, the two sub-tether attachment point vector components with respect to the target's centre of mass are

$$\mathbf{a}_{s1} \equiv \begin{bmatrix} a_{s1,x} \\ a_{s1,y} \end{bmatrix} = \vec{\mathcal{F}}_t \cdot \vec{a}_{s1} \tag{6}$$

$$\mathbf{a}_{s2} \equiv \begin{bmatrix} a_{s2,x} \\ a_{s2,y} \end{bmatrix} = \vec{\mathcal{F}}_t \cdot \vec{a}_{s2}. \tag{7}$$

The angle θ_t represents the rotation about $\vec{I}_z$ to go from $\mathcal{F}_I$ to $\mathcal{F}_t$. Similarly, θ_c describes how $\mathcal{F}_I$ is rotated about $\vec{I}_z$ to obtain $\mathcal{F}_c$. The attitude matrix $\mathbf{A}(\theta)$ is a pure rotation of θ about the $\vec{I}_z$ axis which rotates vector components from a body frame to $\mathcal{F}_I$, given by

$$\mathbf{A}(\theta) = \begin{bmatrix} \cos(\theta) & -\sin(\theta) \\ \sin(\theta) & \cos(\theta) \end{bmatrix} \tag{8}$$

such that vector components are rotated from either body frame to $\mathcal{F}_I$, as follows:

$$\mathbf{x}_I = \mathbf{A}(\theta)\mathbf{x}_b \tag{9}$$

where $\mathbf{x}_b$ are the vector coordinates in a body frame and $\mathbf{x}_I$ are the vector components in $\mathcal{F}_I$.

With the above vector and reference frame definitions, the three degree-of-freedom (i.e., translation along $\vec{I}_x$ and $\vec{I}_y$ and rotation about $\vec{I}_z$) equations of motion for the system can now be presented.

II.A. Translational Motion

The two degree-of-freedom translational equations of motion are governed by Newton's second Law:

$$\mathbf{F} = m\ddot{\mathbf{r}} \tag{10}$$

where $\mathbf{F}$ is the sum of the force vector components acting on any body in $\mathcal{F}_I$, m is the mass of the spacecraft, and $\ddot{\mathbf{r}}$ is the resulting acceleration vector components in $\mathcal{F}_I$.

II.B. Rotational Motion

To model the single degree-of-freedom rotational dynamics, Euler's equations are used[26]

$$\mathbf{J}\dot{\boldsymbol{\omega}} + \boldsymbol{\omega}^{\times}(\mathbf{J}\boldsymbol{\omega}) = \boldsymbol{\tau} \tag{11}$$

where $\mathbf{J}$ is the inertia matrix of the spacecraft, $\boldsymbol{\omega}$ is the angular rate of the spacecraft, and $\boldsymbol{\tau}$ is the external torque applied to the body, all represented in the body-fixed reference frame. It is assumed that the body-fixed frame is aligned with the principal axis of the body, which yields an inertia matrix of

$$\mathbf{J} = \begin{bmatrix} J_{xx} & 0 & 0 \\ 0 & J_{yy} & 0 \\ 0 & 0 & J_{zz} \end{bmatrix} \tag{12}$$

where $J_{ii}\ \forall\ i = \{x, y, z\}$ denotes the principal moments of inertia. Since the simulations and experiments performed are planar, the angular rate vector components will always have the form

$$\boldsymbol{\omega} = \begin{bmatrix} 0 \\ 0 \\ \omega \end{bmatrix} \tag{13}$$

which eliminates the gyroscopic term in Eq. (11) and simplifies it to

$$J_{zz}\dot{\omega} = \tau_z. \tag{14}$$

In order to numerically simulate Eqs. (10) and (14), the forces and torques imparted on the chaser and the target must be quantified. Each tether is herein modeled as a nonlinear massless spring damper system in parallel, as represented in Fig. 2. The following two sections present how the forces and torques are resolved for each TSS configuration. Section II.C presents the equations for the single tether configuration shown in Fig. 1a, and Sec. II.D presents the equations for the sub-tether configuration shown in Fig. 1b.

Downloaded by CARLETON UNIVERSITY on January 24, 2017 | http://arc.aiaa.org | DOI: 10.2514/6.2017-1049

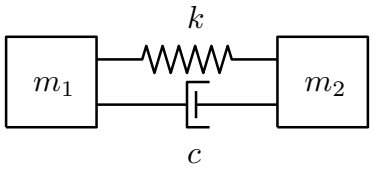

Figure 2. Simple spring-damper system, where two masses are attached via a spring and damper in parallel.

II.C. Single Tether Equations of Motion

According to Fig. 1a, the single tether TSS configuration has one tether that attaches the chaser to the target. Applying Eqs. (10) and (14), the equations of motion applied to this system are, for the passive target:

$$\begin{bmatrix} \ddot{r}_{t,x} \\ \ddot{r}_{t,y} \\ \dot{\omega}_t \end{bmatrix} = \begin{bmatrix} \frac{-F_{s,x}}{m_t} \\ \frac{-F_{s,y}}{m_t} \\ \frac{\tau_t}{J_{zz,t}} \end{bmatrix} \tag{15}$$

and for the active chaser:

$$\begin{bmatrix} \ddot{r}_{c,x} \\ \ddot{r}_{c,y} \\ \dot{\omega}_c \end{bmatrix} = \begin{bmatrix} \frac{F_{s,x}+F_{control,x}}{m_c} \\ \frac{F_{s,y}+F_{control,y}}{m_c} \\ \frac{\tau_c+\tau_{control}}{J_{zz,c}} \end{bmatrix} \tag{16}$$

where:

$$\mathbf{F}_s \equiv \begin{bmatrix} F_{s,x} \\ F_{s,y} \end{bmatrix}, \quad \mathbf{F}_{control} \equiv \begin{bmatrix} F_{control,x} \\ F_{control,y} \end{bmatrix} \tag{17}$$

where $\mathbf{F}_s$ is the components of the force developed in the single tether in $\mathcal{F}_I$, and $\mathbf{F}_{control}$ is the components of the translational control thrust in $\mathcal{F}_I$. Components $\ddot{r}_{t,x}$ and $\ddot{r}_{t,y}$ are the two-dimensional acceleration components of $\ddot{\mathbf{r}}_t$, and $\ddot{r}_{c,x}$ and $\ddot{r}_{c,y}$ are the two-dimensional acceleration components of $\ddot{\mathbf{r}}_c$, all in $\mathcal{F}_I$. Variables $\dot{\omega}_t$ and $\dot{\omega}_c$ represent the angular acceleration of the target and chaser due to the torques imparted to them by the single tether, τ_t and τ_c, in their respective body-fixed frames. Finally, m_t, $J_{zz,t}$, m_c, and $J_{zz,c}$ represent the mass and principal moment of inertia of the target and chaser, respectively. The remainder of this section will be used to determine the tether force $\mathbf{F}_s$, and resultant torques τ_t and τ_c.

The current length of the single tether shown in Fig. 1a is found in $\mathcal{F}_I$ through

$$\mathbf{L}_s = \mathbf{r}_t + \mathbf{A}(\theta_t)\mathbf{a}_t - \mathbf{r}_c - \mathbf{A}(\theta_c)\mathbf{a}_c \tag{18}$$

where $\mathbf{L}_s$ is the components of the tether vector extending from the attachment point on the chaser to the attachment point on the target in $\mathcal{F}_I$, and all other variables have been previously defined. The force developed by the single tether is the sum of the stiffness and viscous forces, calculated as

$$\mathbf{F}_s = \begin{cases} \left[k(\|\mathbf{L}_s\| - L_{s,0}) + c \left(\mathbf{v}_t + \mathbf{A}(\theta_t) \begin{bmatrix} -\omega_t a_{t,y} \\ \omega_t a_{t,x} \end{bmatrix} - \mathbf{v}_c - \mathbf{A}(\theta_c) \begin{bmatrix} -\omega_c a_{c,y} \\ \omega_c a_{c,x} \end{bmatrix} \right) \cdot \frac{\mathbf{L}_s}{\|\mathbf{L}_s\|} \right] \frac{\mathbf{L}_s}{\|\mathbf{L}_s\|}, & \text{for } \|\mathbf{L}_s\| - L_{s,0} > 0 \\ \mathbf{0}, & \text{otherwise} \end{cases} \tag{19}$$

where k is the nonlinear stiffness of the tether material, $L_{s,0}$ is the unstretched length of the tether, c is the damping coefficient of the tether, $\mathbf{v}_t$ and $\mathbf{v}_c$ are the velocities of the target and chaser in $\mathcal{F}_I$, respectively, and ω_t and ω_c are the angular rates of the target and chaser, in their respective body frames. It should be noted that the generated force, $\mathbf{F}_s$, is non-zero only when the tether is stretched.

The calculation to determine the torque that the single tether delivers to each spacecraft is performed in $\mathcal{F}_t$ and $\mathcal{F}_c$. Therefore, the tether force vector components found in Eq. (19) must be rotated into each body

Downloaded by CARLETON UNIVERSITY on January 24, 2017 | http://arc.aiaa.org | DOI: 10.2514/6.2017-1049

frame using the attitude matrix, i.e.,

$$\mathbf{F}_s^t \equiv \begin{bmatrix} F_{s,x}^t \\ F_{s,y}^t \end{bmatrix} = \mathbf{A}(\theta_t)^{\mathrm{T}} \mathbf{F}_s \tag{20}$$

$$\mathbf{F}_s^c \equiv \begin{bmatrix} F_{s,x}^c \\ F_{s,y}^c \end{bmatrix} = \mathbf{A}(\theta_c)^{\mathrm{T}} \mathbf{F}_s \tag{21}$$

where $\mathbf{F}_s^t$ is the single tether force expressed in $\mathcal{F}_t$ and $\mathbf{F}_s^c$ is the same in $\mathcal{F}_c$. The torque that the single tether delivers to each spacecraft is found via

$$\tau_t = a_{t,y} F_{s,x}^t - a_{t,x} F_{s,y}^t \tag{22}$$

$$\tau_c = a_{c,x} F_{s,y}^c - a_{c,y} F_{s,x}^c. \tag{23}$$

In order to numerically simulate the motion, the forces and torques generated by the tether and control actuators are used with Eqs. (15) and (16). The following section presents the sub-tether TSS configuration equations of motion.

II.D. Sub-Tether Equations of Motion

The sub-tether configuration has a main tether that attaches to the chaser and branches into two sub-tethers that are attached to the target at various locations, as shown in Fig. 1b. The point where the main tether branches into two sub-tethers is denoted the *junction* and is treated as a small point mass. Applying Eqs. (10) and (14) to this system, the equations of motion are, for the target:

$$\begin{bmatrix} \ddot{r}_{t,x} \\ \ddot{r}_{t,y} \\ \dot{\omega}_t \end{bmatrix} = \begin{bmatrix} \frac{-(F_{s1,x}+F_{s2,x})}{m_t} \\ \frac{-(F_{s1,y}+F_{s2,y})}{m_t} \\ \frac{\tau_{t,s1}+\tau_{t,s2}}{J_{zz,t}} \end{bmatrix} \tag{24}$$

for the junction:

$$\begin{bmatrix} \ddot{r}_{j,x} \\ \ddot{r}_{j,y} \end{bmatrix} = \begin{bmatrix} \frac{F_{s1,x}+F_{s2,x}-F_{m,x}}{m_j} \\ \frac{F_{s1,y}+F_{s2,y}-F_{m,y}}{m_j} \end{bmatrix} \tag{25}$$

and for the chaser:

$$\begin{bmatrix} \ddot{r}_{c,x} \\ \ddot{r}_{c,y} \\ \dot{\omega}_c \end{bmatrix} = \begin{bmatrix} \frac{F_{m,x}+F_{control,x}}{m_c} \\ \frac{F_{m,y}+F_{control,y}}{m_c} \\ \frac{\tau_{c,m}+\tau_{control}}{J_{zz,c}} \end{bmatrix} \tag{26}$$

where:

$$\mathbf{F}_m \equiv \begin{bmatrix} F_{m,x} \\ F_{m,y} \end{bmatrix}, \quad \mathbf{F}_{s1} \equiv \begin{bmatrix} F_{s1,x} \\ F_{s1,y} \end{bmatrix}, \quad \mathbf{F}_{s2} \equiv \begin{bmatrix} F_{s2,x} \\ F_{s2,y} \end{bmatrix} \tag{27}$$

where $\mathbf{F}_m$ represents the force vector components of the main tether in $\mathcal{F}_I$, $\mathbf{F}_{s1}$ and $\mathbf{F}_{s2}$ represent the force vector components of the two sub-tethers in $\mathcal{F}_I$, $\tau_{t,s1}$ and $\tau_{t,s2}$ denote the torques imparted to the target due to the two sub-tethers in $\mathcal{F}_t$, and $\tau_{c,m}$ denotes the torque applied to the chaser from the main tether segment in $\mathcal{F}_c$. The remainder of this section will present the derivation of $\mathbf{F}_m$, $\mathbf{F}_{s1}$, $\mathbf{F}_{s2}$, $\tau_{c,m}$, $\tau_{t,s1}$, and $\tau_{t,s2}$.

The main tether vector, $\vec{L}_m$, attaches the chaser to the junction. The two sub-tether vectors, $\vec{L}_{s1}$ and $\vec{L}_{s2}$, extend from the junction to the two attachment points on the target. The tether vector coordinates in $\mathcal{F}_I$ are given by

$$\mathbf{L}_m = \mathbf{r}_j - \mathbf{r}_c - \mathbf{A}(\theta_c)\mathbf{a}_c \tag{28}$$

$$\mathbf{L}_{s1} = \mathbf{r}_t + \mathbf{A}(\theta_t)\mathbf{a}_{s1} - \mathbf{r}_j \tag{29}$$

$$\mathbf{L}_{s2} = \mathbf{r}_t + \mathbf{A}(\theta_t)\mathbf{a}_{s2} - \mathbf{r}_j \tag{30}$$

Downloaded by CARLETON UNIVERSITY on January 24, 2017 | http://arc.aiaa.org | DOI: 10.2514/6.2017-1049

where all variables have been previously defined. The resulting forces in the main tether and sub-tethers are:

$$\mathbf{F}_m = \begin{cases} \left[k(\|\mathbf{L}_m\| - L_{m,0}) + c \left(\mathbf{v}_j - \mathbf{v}_c - \mathbf{A}(\theta_c) \begin{bmatrix} -\omega_c a_{c,y} \\ \omega_c a_{c,x} \end{bmatrix} \right) \cdot \frac{\mathbf{L}_m}{\|\mathbf{L}_m\|} \right] \frac{\mathbf{L}_m}{\|\mathbf{L}_m\|}, & \text{for } \|\mathbf{L}_m\| - L_{m,0} > 0 \\ \mathbf{0}, & \text{otherwise} \end{cases} \tag{31}$$

$$\mathbf{F}_{s1} = \begin{cases} \left[k(\|\mathbf{L}_{s1}\| - L_{s1,0}) + c \left(\mathbf{v}_t + \mathbf{A}(\theta_t) \begin{bmatrix} -\omega_t a_{s1,y} \\ \omega_t a_{s1,x} \end{bmatrix} - \mathbf{v}_j \right) \cdot \frac{\mathbf{L}_{s1}}{\|\mathbf{L}_{s1}\|} \right] \frac{\mathbf{L}_{s1}}{\|\mathbf{L}_{s1}\|}, & \text{for } \|\mathbf{L}_{s1}\| - L_{s1,0} > 0 \\ \mathbf{0}, & \text{otherwise} \end{cases} \tag{32}$$

$$\mathbf{F}_{s2} = \begin{cases} \left[k(\|\mathbf{L}_{s2}\| - L_{s2,0}) + c \left(\mathbf{v}_t + \mathbf{A}(\theta_t) \begin{bmatrix} -\omega_t a_{s2,y} \\ \omega_t a_{s2,x} \end{bmatrix} - \mathbf{v}_j \right) \cdot \frac{\mathbf{L}_{s2}}{\|\mathbf{L}_{s2}\|} \right] \frac{\mathbf{L}_{s2}}{\|\mathbf{L}_{s2}\|}, & \text{for } \|\mathbf{L}_{s2}\| - L_{s2,0} > 0 \\ \mathbf{0}, & \text{otherwise} \end{cases} \tag{33}$$

where $L_{m,0}$, $L_{s1,0}$, and $L_{s2,0}$ are the unstretched lengths of the main tether and sub-tethers, and $\mathbf{v}_j$ is the velocity components of the junction in $\mathcal{F}_I$. The resulting forces, $\mathbf{F}_m$, $\mathbf{F}_{s1}$, and $\mathbf{F}_{s2}$ are calculated in $\mathcal{F}_I$, and are only non-zero when the tethers are stretched. The torque delivered to each spacecraft is expressed in its body frame. Therefore, as with the single tether configuration, the tether forces must be rotated into the appropriate body-fixed reference frame, through:

$$\mathbf{F}_m^c \equiv \begin{bmatrix} F_{m,x}^c \\ F_{m,y}^c \end{bmatrix} = \mathbf{A}(\theta_c)^{\mathrm{T}} \mathbf{F}_m \tag{34}$$

$$\mathbf{F}_{s1}^t \equiv \begin{bmatrix} F_{s1,x}^t \\ F_{s1,y}^t \end{bmatrix} = \mathbf{A}(\theta_t)^{\mathrm{T}} \mathbf{F}_{s1} \tag{35}$$

$$\mathbf{F}_{s2}^t \equiv \begin{bmatrix} F_{s2,x}^t \\ F_{s2,y}^t \end{bmatrix} = \mathbf{A}(\theta_t)^{\mathrm{T}} \mathbf{F}_{s2} \tag{36}$$

where, $\mathbf{F}_m^c$ is the main tether force vector components in $\mathcal{F}_c$, and $\mathbf{F}_{s1}^t$ and $\mathbf{F}_{s2}^t$ are the force vector components of the two sub-tethers in $\mathcal{F}_t$. The resulting torques on the spacecraft are calculated as follows:

$$\tau_{t,s1} = a_{s1,y} F_{s1,x}^t - a_{s1,x} F_{s1,y}^t \tag{37}$$

$$\tau_{t,s2} = a_{s2,y} F_{s2,x}^t - a_{s2,x} F_{s2,y}^t \tag{38}$$

$$\tau_{c,m} = a_{c,x} F_{m,y}^c - a_{c,y} F_{m,x}^c \tag{39}$$

and are used with Eqs. (31)-(33) in Eqs. (24)-(26) to simulate the motion. A nonlinear tether model is developed in the following section.

II.E. Non-linear Tether Model

A braided elastic tether material consisting of 56% plolyester and 44% rubber was obtained for use in experiments. A flexible tether material with a low stiffness was chosen to allow for measurable tether stretches with short tethers in a laboratory setting. By suspending known masses from a tether segment and measuring the resulting stretch, it was found that the tether material has a non-linear stiffness. The three sub-tether segments are identical in length and their stiffness model is shown in Figure 3a. The single tether stiffness model is shown in Figure 3b. For a given tether stretch, the corresponding stiffness in the tether is found by interpolating the experimental data using the *spline* function in MATLAB/Simulink. The tether damping was assumed to be constant, as a reliable technique for characterizing its non-linearity was not available.

With the dynamics and tethers modeled, numerical simulations can be performed.

Downloaded by CARLETON UNIVERSITY on January 24, 2017 | http://arc.aiaa.org | DOI: 10.2514/6.2017-1049

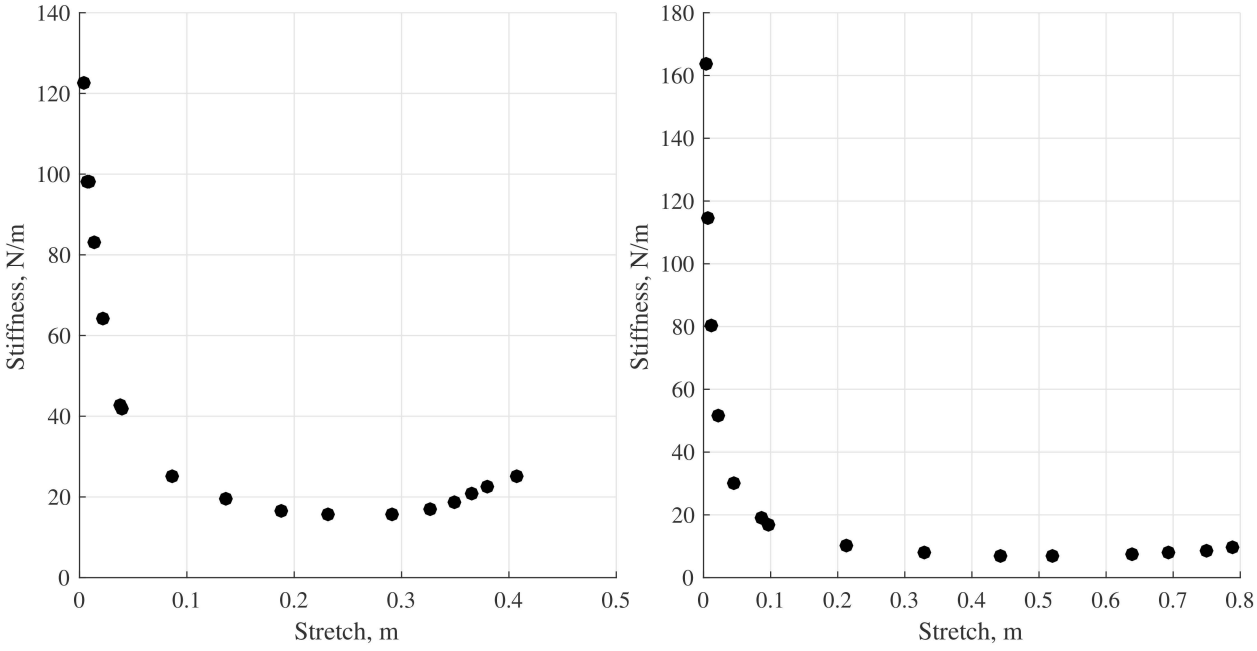

(a) Sub-tether (b) Single tether

Figure 3. Experimental non-linear tether stiffness model, generated by hanging known masses from each tether and measuring the resulting stretch.

III. Numerical Simulations

In order to maintain control of a target, tension in the tethers is required.[25] Two main techniques for generating tension in the tethers are herein proposed. Those are: 1) commanding the chaser to thrust away from the target, creating tension in the tethers that regulate the attitude of the target, and 2) spinning the entire TSS such that the centripetal force provides the tension required to stabilize the target. Two numerical simulations are performed for each tether configuration, to demonstrate the effectiveness of these two modes of stabilization available for a TSS. The parameters in Table 1 are held constant for each simulation. A standard

Table 1. Initial conditions and TSS parameters for all simulations and experiments.

Parameter	Value	Parameter	Value	Parameter	Value
$J_{zz,t}$, kg $\cdot$ m^2	0.22	$L_{m,0}$, m	0.28	c_{single}, $\frac{\text{N}\cdot\text{s}}{\text{m}}$	3.0
$J_{zz,c}$, kg $\cdot$ m^2	0.30	$L_{s1,0}$, m	0.28	c_{sub}, $\frac{\text{N}\cdot\text{s}}{\text{m}}$	0.9
m_t, kg	12.19	$L_{s2,0}$, m	0.28	$K_{P,\theta}$	0.33
m_c, kg	17.24	$L_{s,0}$, m	0.54	$K_{D,\theta}$	0.56
m_j, kg	0.01	$\mathbf{a}_c$, m	[0.135;-0.009]	$\mathbf{K}_P$	$19.1\mathbf{I}_{2\times2}$
θ_c, deg	180	$\mathbf{a}_{s1}$, m	[0.110;0.127]	$\mathbf{K}_D$	$32.7\mathbf{I}_{2\times2}$
θ_t, deg	0	$\mathbf{a}_{s2}$, m	[0.113;-0.094]		
Time Step, s	0.004	$\mathbf{a}_t$, m	[0.110;0.016]		

proportional-derivative controller is used for the position and attitude control of the chaser platform. The control actuation is governed by

$$\mathbf{F}_{control} = \mathbf{K}_P[\mathbf{r}_{des}(t) - \mathbf{r}_c(t)] + \mathbf{K}_D[\dot{\mathbf{r}}_{des}(t) - \dot{\mathbf{r}}_c(t)] \tag{40}$$

Downloaded by CARLETON UNIVERSITY on January 24, 2017 | http://arc.aiaa.org | DOI: 10.2514/6.2017-1049

where $\mathbf{r}_{des}$ is the desired chaser position in $\mathcal{F}_I$, $\mathbf{K}_P$ is the proportional gain matrix and $\mathbf{K}_D$ is the derivative gain matrix, as listed in Table 1. The attitude controller is similarly:

$$\tau_{control} = K_{P,\theta}[\theta_{des}(t) - \theta(t)] + K_{P,\theta}[\dot{\theta}_{des}(t) - \dot{\theta}(t)] \tag{41}$$

where $\theta_{des}(t)$ is the desired angle of the chaser as a function of time, and $K_{P,\theta}$ and $K_{D,\theta}$ represent the constant proportional and derivative control gains, respectively.

The details and results of each simulation case are presented in the following subsections. Results of the simulations include time histories of the target tether angle, and the target angular rate, and the total angular momentum of the system. Figure 4 depicts the target tether angle, defined as a positive angle between $\vec{T}_x$ and the tether. A goal of the stabilization process is to regulate the tether angle, reduce the angular rates, and dissipate angular momentum from the system.

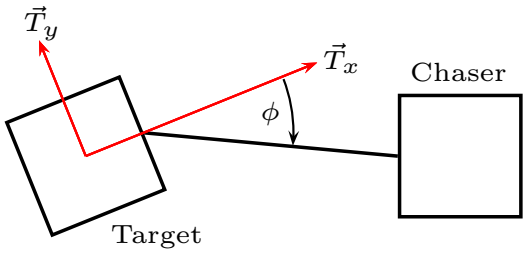

Figure 4. Positive angle ϕ represents the current angle between $\vec{T}_x$ and the tether. The sub-tether configuration uses an imaginary single tether to calculate the tether angle.

III.A. Thrust Stabilization

This section presents a technique for stabilizing a spinning target by continuously accelerating away from it. The acceleration maintains tension in the tethers which regulates the attitude of the target. The numerical simulation is performed in MATLAB/Simulink with initial conditions listed in Table 2. Both spacecraft are at rest and aligned such that all tethers are initially just tight. At time $t = 2$, the target uses its thrusters to reach an angular rate of ω_{t0}. At the same time, the chaser initiates its control system to provide constant acceleration away from the target. To achieve the constant acceleration of the chaser, the desired

Table 2. Initial conditions for thrust stabilization simulations and experiments.

Parameter	Value	Parameter	Value
$\mathbf{r}_t$, m	[0.35;1.19]	$\mathbf{v}_t$, m/s	[0;0]
$\mathbf{r}_c$, m	[1.10;1.20]	$\mathbf{v}_c$, m/s	[0;0]
ω_{t0}, deg/s	10	Simulation Length, s	100

position, $\mathbf{r}_{des}(t)$, is fed to the chaser's position control system and is varied through time to reach the position $\mathbf{r}_f = [3.10; 1.20]$ m in 20 s. Specifically, it is varied through

$$\mathbf{r}_{des}(t) = \mathbf{r}_0 + \mathbf{d}\frac{t^2}{2} \tag{42}$$

where $\mathbf{d}$ is the desired constant acceleration, and t is the time. The desired acceleration is calculated through

$$\mathbf{d} = \frac{2(\mathbf{r}_f - \mathbf{r}_0)}{t^2} \tag{43}$$

where $\mathbf{r}_0$ and $\mathbf{r}_f$ are the initial and final positions of the chaser in $\mathcal{F}_I$, and t is the time taken to move from $\mathbf{r}_0$ to $\mathbf{r}_f$. The attitude control system on the chaser is set to continually hold its initial attitude at θ_c. Both

Downloaded by CARLETON UNIVERSITY on January 24, 2017 | http://arc.aiaa.org | DOI: 10.2514/6.2017-1049

Downloaded by CARLETON UNIVERSITY on January 24, 2017 | http://arc.aiaa.org | DOI: 10.2514/6.2017-1049

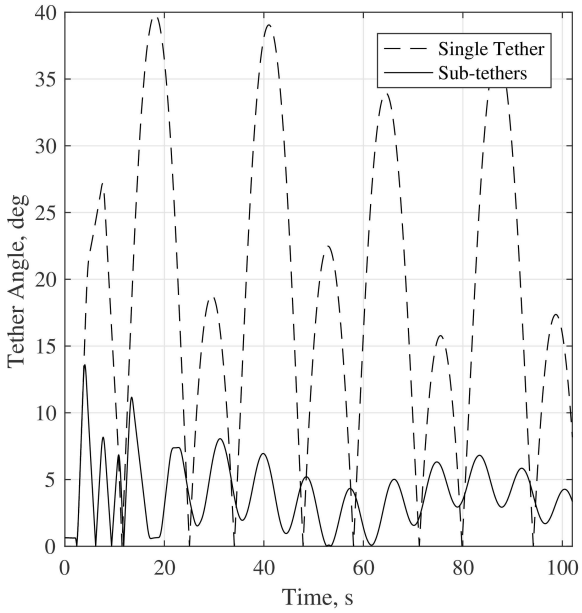

(a) Target tether angle

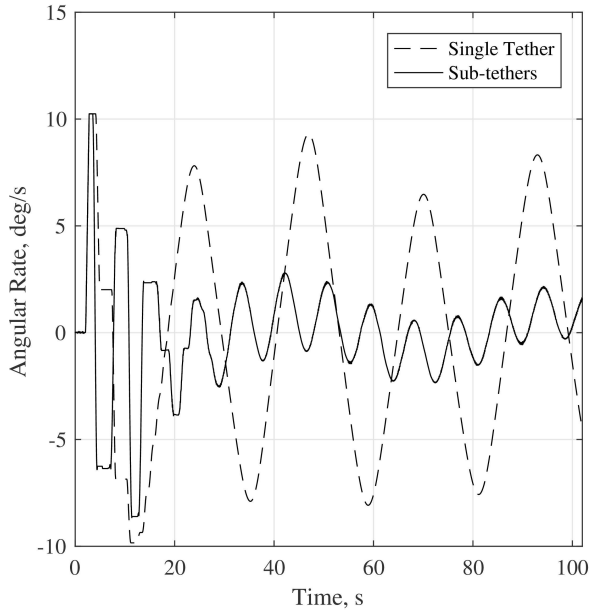

(b) Target angular rate

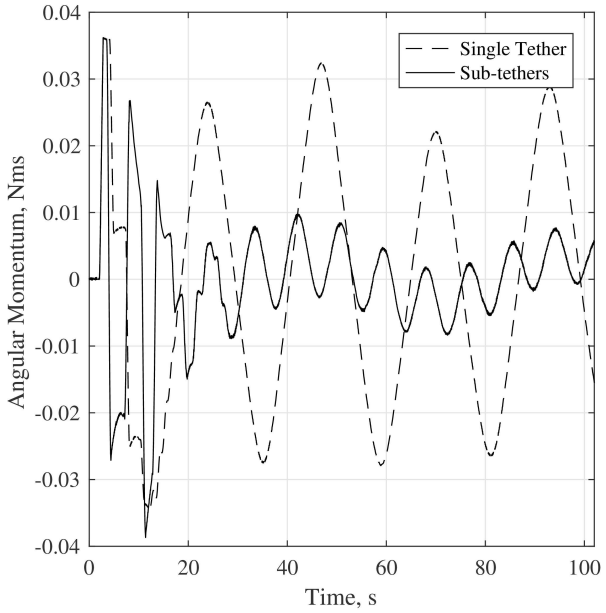

(c) Total angular momentum

Figure 5. Resulting simulated TSS motion for thrust stabilization, comparing the two tether configurations.

TSS configurations were simulated with identical initial conditions such that the two scenarios can readily be compared.

Figure 5 presents the results of the numerical simulation. Figure 5a shows the tether angle as a function of time. One of the objectives of the attitude stabilization strategy is to reduce this angle to zero. The proposed sub-tether configuration results in a tether angle that is considerably smaller than the single tether configuration for the same initial conditions.

Figure 5b shows the angular rate of the target as a function of time. Both TSS configurations regulate the angular rate of the target towards zero, but the sub-tether configuration does so significantly quicker. Stabilizing a target quickly after capture is highly desirable, and this test scenario demonstrates how simply altering the tether configuration passively enhances the stabilization ability of the system. The proposed

sub-tether configuration better exploits the damping properties of the tethers compared to the single tether configuration. Tether damping is the mechanism through which angular momentum is removed from the system. Figure 5c shows the total angular momentum of the system over time. The sub-tether configuration is more effective at dissipating angular momentum than the single tether configuration.

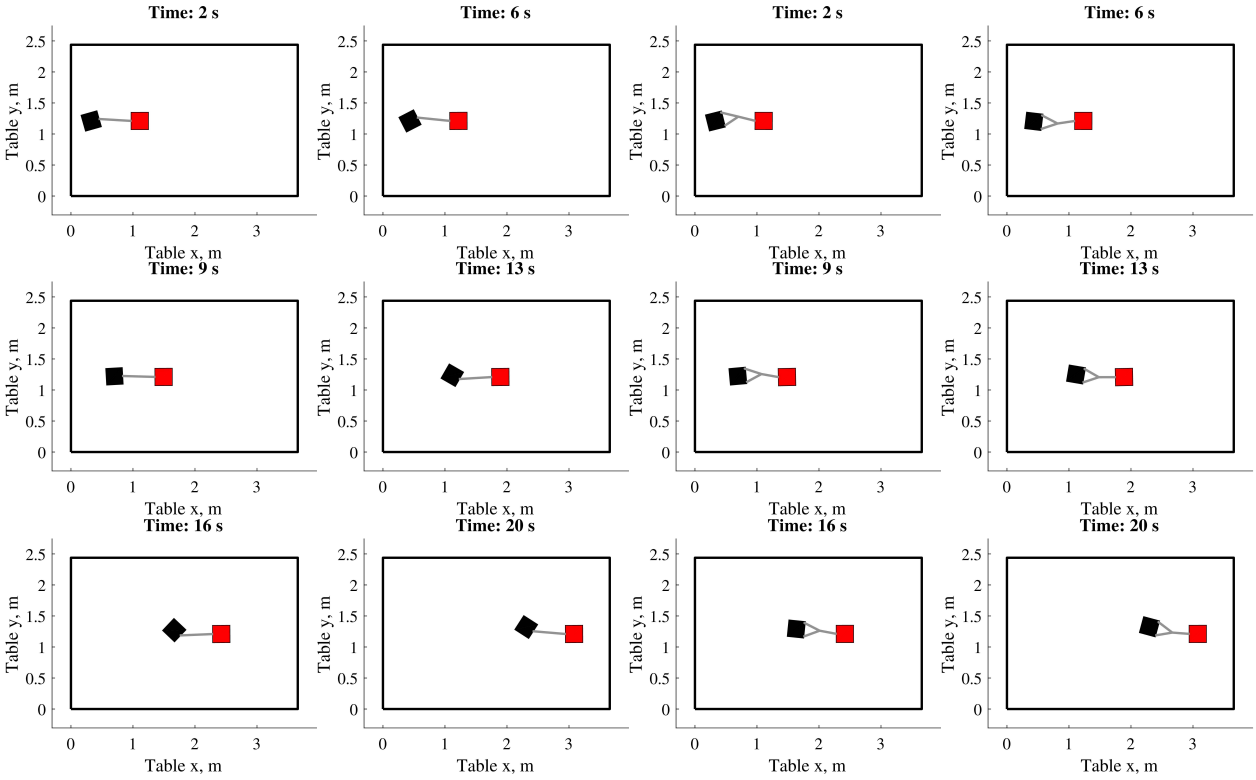

(a) Single tether (b) Sub-tether

Figure 6. Snapshots of an animation of the resulting motion for the thrust stabilization simulation. The red spacecraft is the chaser and the black is the target. The single tether and sub-tethers are shown in gray.

Figure 6 shows snapshots of an animation of the motion, which can be found at https://goo.gl/lzgziR for the single tether configuration, and at https://goo.gl/YgMvr2 for the sub-tether configuration. The red box represents the chaser and the black box represents the target. The single tether configuration is shown on the left and the sub-tether configuration is shown on the right at each time step. The large black rectangle represents the size of the granite table that will be used for the experiments. Notice how at each frame of the animation, the sub-tether configuration leads the target to have a smaller tether angle than the single tether configuration.

Section III.B simulates another mode of maintaining tether tension to stabilize a spinning target.

III.B. TSS Spin Stabilization

This section demonstrates another mode for stabilizing the target. That is, to initiate a TSS spin such that the chaser and target are spinning about the barycentre of the TSS. The goal of this spin technique is to use the centripetal force generated by the rotation to maintain tension in the tethers and regulate the attitude of the uncooperative target. The main benefit of this technique is that once initiated, it does not consume fuel. A disadvantage to TSS spin stabilization is that the target and chaser will have a residual angular rate with respect to $\mathcal{F}_I$ even once the target's attitude has been regulated with respect to $\mathcal{F}_c$. However, once the target tether angle has been significantly reduced, deorbiting can still be performed. It is possible that a TSS spin to stabilize a target may be performed initially to passively remove some angular momentum from the target before a deorbiting burn is performed. Initial conditions for the simulation are shown in Table 3. The translational control system is not used on the chaser for this simulation. The spacecraft are initially positioned such that all tethers are barely under tension. The attitude control system is used to command

Downloaded by CARLETON UNIVERSITY on January 24, 2017 | http://arc.aiaa.org | DOI: 10.2514/6.2017-1049

Table 3. Initial conditions for TSS spin simulations and experiments.

Parameter	Value	Parameter	Value
$\mathbf{r}_t$, m	[2.02;0.74]	$\mathbf{v}_t$, m/s	[0;-0.3]
$\mathbf{r}_c$, m	[2.80;0.75]	$\mathbf{v}_c$, m/s	[0;0.2]
ω_{t0}, deg/s	79	Simulation Length, s	30

the chaser to continually point its $\vec{C}_x$ axis toward the target. The desired chaser angle, θ_{des}, used in the control system is calculated as follows

$$\theta_{des} = \tan^{-1}\left(\frac{r_{t,y} - r_{c,y}}{r_{t,x} - r_{c,x}}\right) \tag{44}$$

where $r_{t,y}$ and $r_{c,y}$ are the y components of $\mathbf{r}_t$ and $\mathbf{r}_c$, respectively, and $r_{t,x}$ and $r_{c,x}$ are the x components of $\mathbf{r}_t$ and $\mathbf{r}_c$. The target is given an angular rate of ω_{t0} at $t = 2$ s. Plots of the resulting motion are shown in Fig. 7.

Simulation results show how spinning the TSS is a valid technique for stabilizing an uncooperative spacecraft, and how the proposed sub-tether configuration is more efficient than the single tether configuration. Figures 7a and 7b show that while the single tether is reducing the tether angle and angular rate of the target, it does so much slower than the sub-tether configuration. The angular rate in Fig. 7b does not tend toward zero but converges to the spin rate of the TSS, as previously discussed. A similar trend is observed in the total angular momentum plot in Fig. 7c. Snapshots of the simulated motion are shown in Fig. 8, and an animation can be found at https://goo.gl/8y8H31 for the single tether configuration and https://goo.gl/tOsIzu for the sub-tether configuration. Notice how over time, the sub-tether configuration keeps the target tether angle very low.

To validate the numerical simulations, experiments are performed. The following section describes the experimental laboratory setup, and presents and discusses experimental results.

IV. Experimental Validation

To validate the numerical simulations, experiments are performed in the Spacecraft Robotics and Control Laboratory (SRCL) at Carleton University. A planar gravity-offset testbed is used, where two spacecraft platforms are tethered together on a flat granite surface. Air bearings are used to provide a near friction-free planar environment. Small air thrusters expel compressed air to provide translational and attitude motion. A reaction wheel is also used for attitude control. All actuators are interfaced with a Raspberry Pi 3 that runs the control software. The control software is prepared in the MATLAB/Simulink environment and compiled into a binary that is executed on the Pi. Developing the software in the MATLAB/Simulink environment allows for the identical software to be simulated and used in experiment. Wireless communication is provided between a ground station computer and the Pi via Wi-Fi. The ground station uploads software wirelessly to the Pi, starts and stops experiments, and transmits position and attitude data to the Pi in real-time for use in the feedback control system. The position and attitude data is obtained from 8 cameras tracking LEDs that are fixed to each spacecraft platform. The two TSS configurations numerically simulated in this paper are replicated in experiments.

Figure 9 shows the two Spacecraft Proximity Operations Testbed (SPOT) spacecraft platforms built in Carleton's SRCL. The chaser and target used in the experiment are nearly identical. The simulation cases presented in Sec. III were chosen such that they are replicable experimentally. Experiment properties are the same as in Table 1.

The experiment design consists of two SPOT platforms placed on the flat table and tethered together using the tethers that were modeled in simulation. Figure 10 shows the two SPOT spacecraft tethered together on the flat table in the sub-tether configuration.

The platforms sit on the table until a strong lock has been acquired on the LEDs by the camera tracking system. Following this, the platforms begin to float and spend 60 seconds moving to the desired initial

Downloaded by CARLETON UNIVERSITY on January 24, 2017 | http://arc.aiaa.org | DOI: 10.2514/6.2017-1049

Downloaded by CARLETON UNIVERSITY on January 24, 2017 | http://arc.aiaa.org | DOI: 10.2514/6.2017-1049

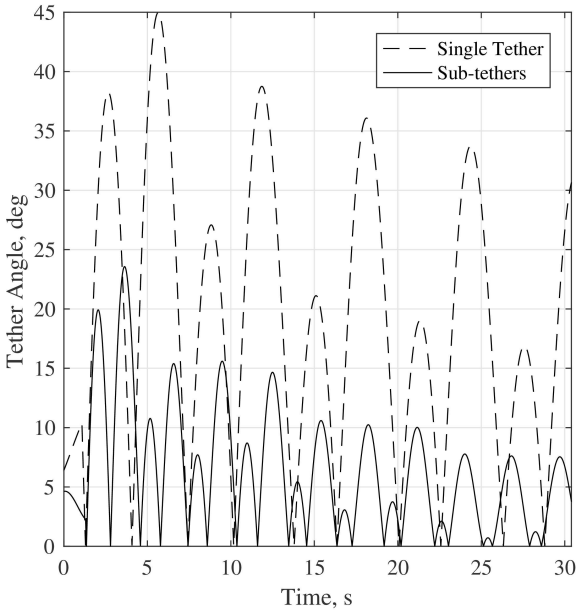

(a) Target tether angle

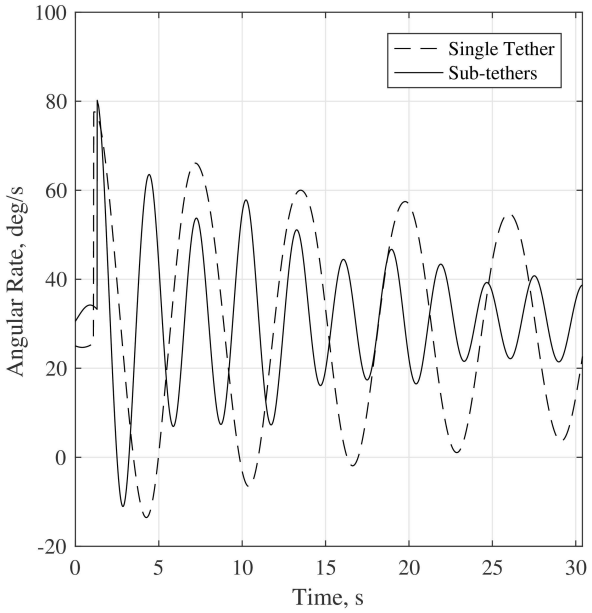

(b) Target angular rate

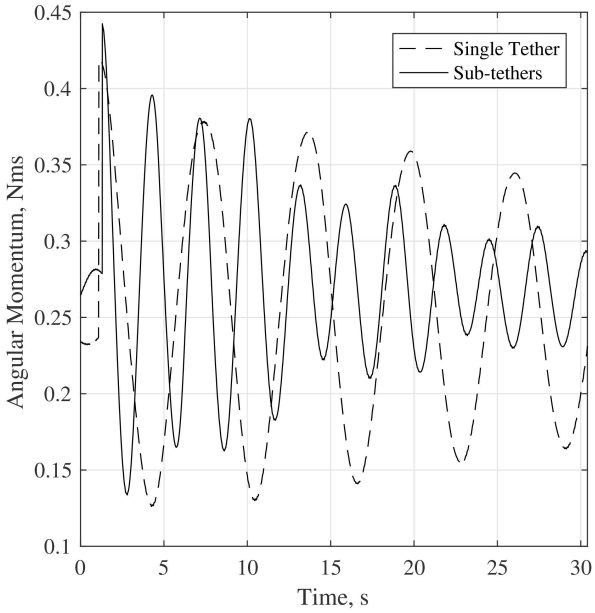

(c) Total angular momentum

Figure 7. Resulting simulated motion for TSS spin stabilization, comparing the two tether configurations.

position on the table and come to rest.

To establish the spinning and tumbling initial conditions for the TSS spin technique discussed in Sec. III.B, both spacecraft exert equal thrust perpendicular to the line joining the two SPOT platforms, in opposite directions, for 10 seconds. This establishes a TSS spin about the barycentre of the system. Once the spin has been initiated, the operator manually provides a disturbance to the target to initiate a tumbling motion. This creates the initial conditions listed in Table 3. Once the tumbling has been initiated, the target becomes fully passive, and the chaser uses its thrusters solely to maintain its $\vec{C}_x$ axis pointing at the target. The system coasts for 35 seconds, drifting due to the slight slope in the table, while the tethers and sub-tethers reduce the tether angle of the target and dissipate some of the angular momentum in the system. A video of the single tether experiment can be found at: https://goo.gl/xoXGIB. Results from the single tether

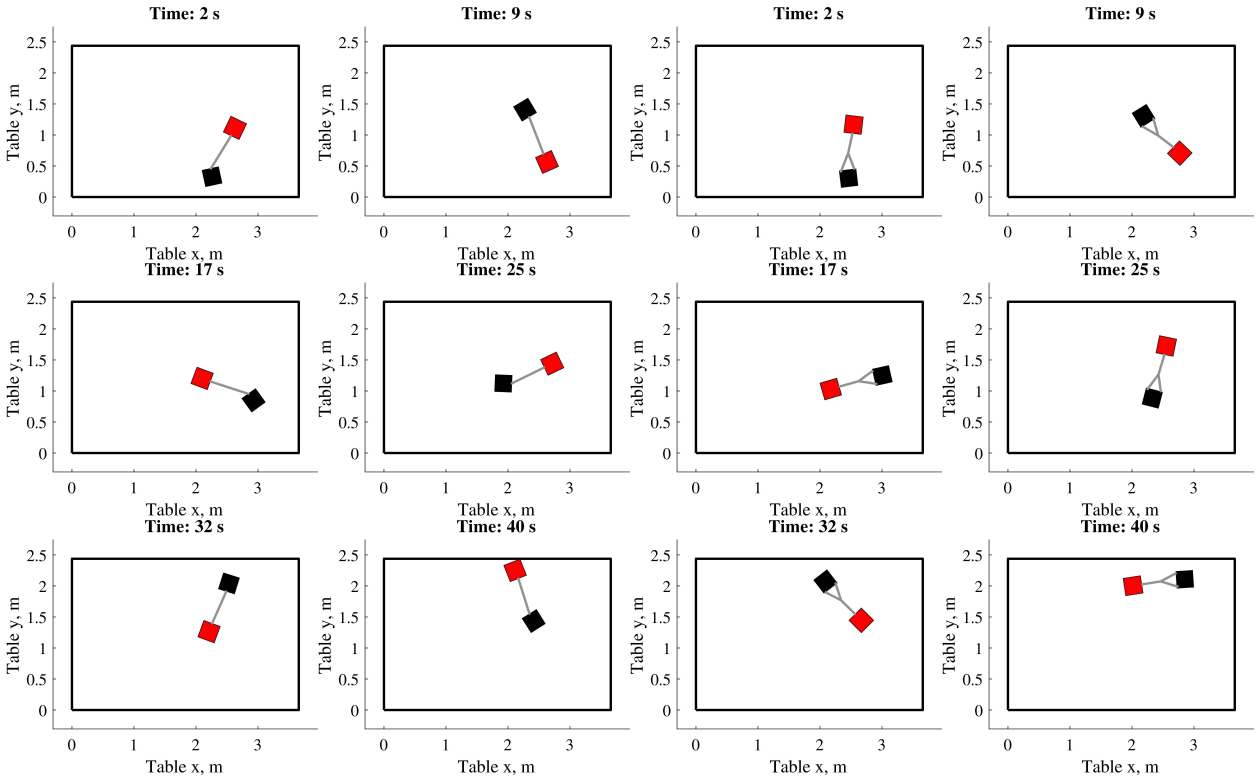

(a) Single tether (b) Sub-tether

Figure 8. Snapshots of an animation of the resulting motion for the TSS spin stabilization simulation. The red spacecraft is the chaser and the black is the target. The single tether and sub-tethers are shown in gray.

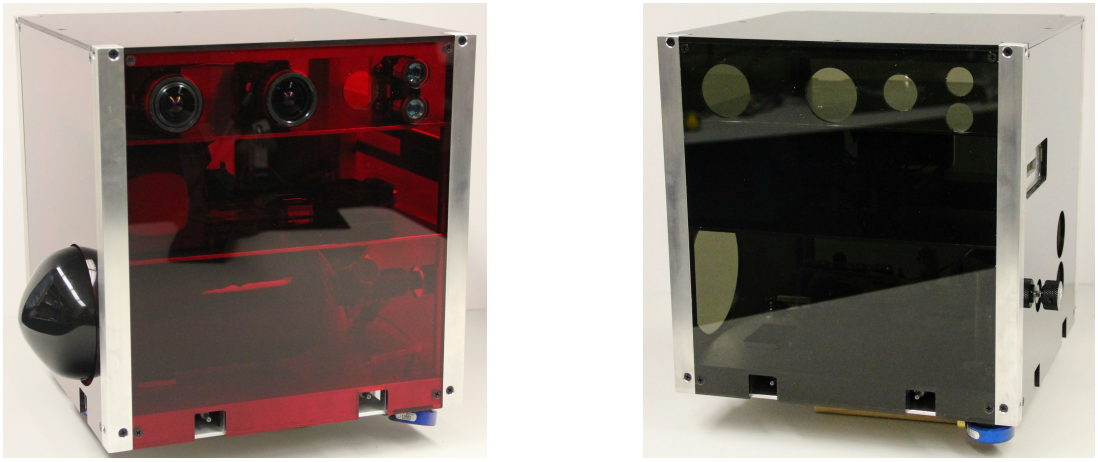

(a) Chaser (b) Target

Figure 9. SPOT platforms built in Carleton's SRCL.

TSS spin experiments are compared to simulated results in Fig. 11. These data constitute the first published results from the SRCL.

The tether angle described in Fig. 4 is shown in Fig. 11a. The similarities between the simulated and experimental results are obvious, with only small discrepancies in the amplitude of the oscillations. These discrepancies may be due to numerous sources, including: uncertainties in mass properties of SPOT, an inaccurate tether model, or unmodeled effects such as drag or friction between SPOT and the flat table. The

Downloaded by CARLETON UNIVERSITY on January 24, 2017 | http://arc.aiaa.org | DOI: 10.2514/6.2017-1049

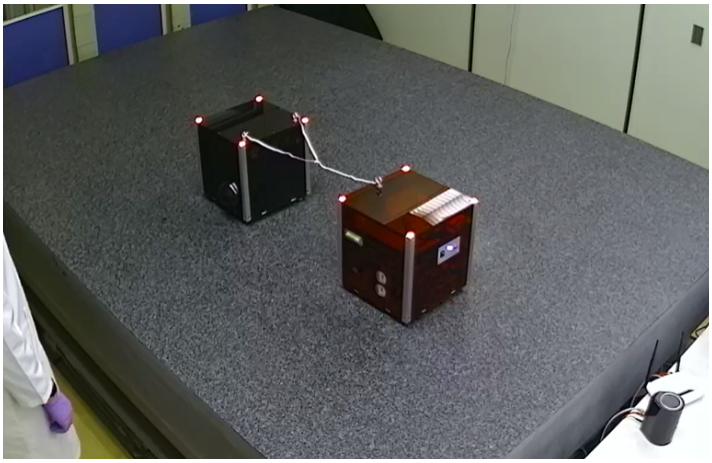

Figure 10. Two SPOT platforms tethered together on the planar gravity-offset testbed at Carleton's SRCL.

Downloaded by CARLETON UNIVERSITY on January 24, 2017 | http://arc.aiaa.org | DOI: 10.2514/6.2017-1049

plot of the angular rate over time, shown in Fig. 11b, also has excellent correlation. The angular momentum of the entire system is calculated and shown in Fig. 11c, showing that the initial angular momentum due to the tumbling of the target slowly dissipates such that the total angular momentum tends towards the steady state angular momentum of the TSS spinning about its barycentre. The angular momentum in the experiment tends toward a lower final angular momentum quantity than in simulation, and is attributed to the unmodeled air drag and residual friction slowing down the two spacecraft from spinning about the barycentre of the TSS. The experimental results successfully validate the presented single tether model.

A video of the sub-tether experiment can be found at https://goo.gl/PXBtju. Experimental results are compared to simulated results in Fig. 12.

The experiment and simulation are well correlated once again. Figure 12a shows minor tether angle discrepancies in amplitude but a nearly identical trend. The oscillations quickly decay to around 5 deg in 30 seconds, indicating the target tumbling has been quickly regulated. The target angular rate shown in Fig. 12b show a quick decay that converges to the TSS spin rate. In fact, the steady state angular rate is slightly lower in experiment as compared to simulation, which is again likely due to drag and friction slowing the TSS spin rate over time. The tethers effectively dissipate the angular momentum in the system, as demonstrated in Fig. 12c. The sub-tether damping quickly dissipates the angular momentum in the system that is a result of the tumbling motion of the target. The strong correlation between experiment and simulation results demonstrate the validity and effectiveness of the proposed sub-tether configuration.

The single tether and sub-tether experimental responses are compared in Fig. 13. All three plots show that the sub-tether configuration significantly outperforms the single tether configuration when it comes to detumbling a passive target, all else being equal for all practical purposes. Both the tether angle, shown in Fig. 13a, and the target angular rate, shown in Fig. 13b are significantly reduced using the sub-tether configuration, but are barely reduced from their initial condition using a single tether configuration. This demonstrates how using a sub-tether configuration passively enhances the stabilizing ability of the TSS. Based on the authors' knowledge, these results constitute the first experimental results of using a chaser to regulate a tumbling target using tethers.

Experiments for the thrust stabilizing technique discussed in Sec. III.A were performed, but abandoned due to the exhaust from the chaser spacecraft interacting with the target which lead to significant unmodeled effects.

V. Conclusions

One of the major difficulties in capturing space debris is controlling it in the period immediately after capture, due to their residual angular momentum. While there are multiple capture techniques available, this paper focused on the tethered net or harpoon approach to create a Tethered Spacecraft System. This paper examined the debris stabilization phase of the mission immediately after the TSS was established, which must be completed before safe towing operations to a disposal orbit or into the atmosphere can begin.

Downloaded by CARLETON UNIVERSITY on January 24, 2017 | http://arc.aiaa.org | DOI: 10.2514/6.2017-1049

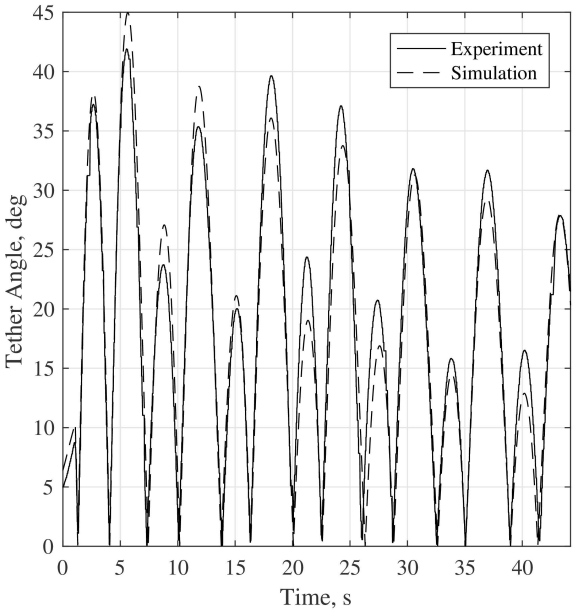

(a) Target tether angle

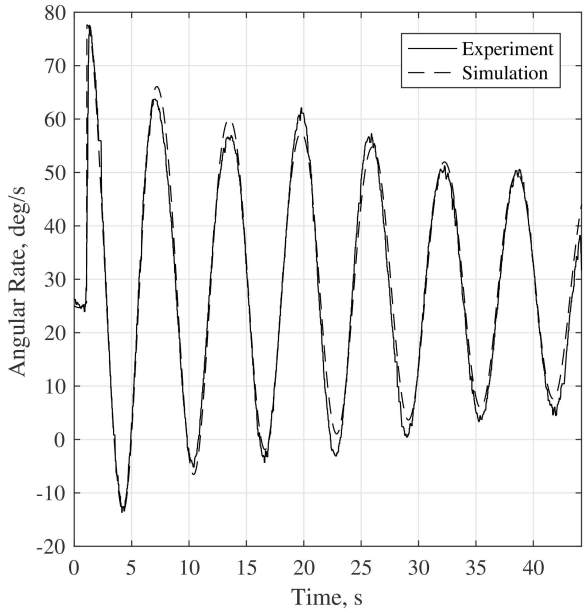

(b) Target angular rate

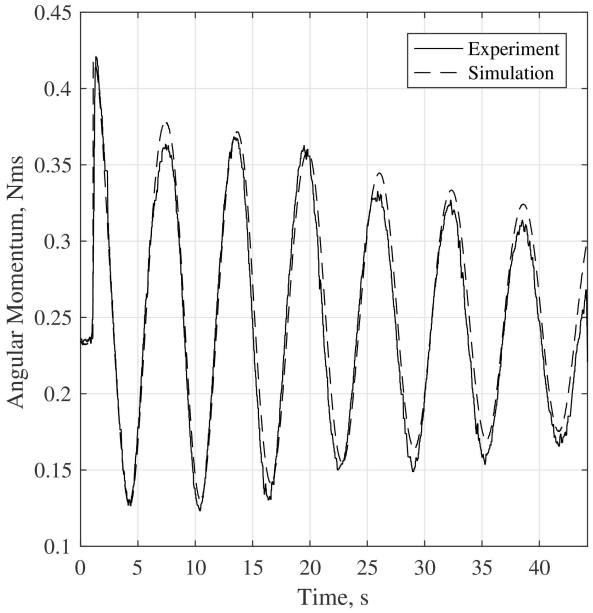

(c) Total angular momentum

Figure 11. Comparing experimental and simulated response for the TSS spin stabilization technique with a single tether.

Two TSS configurations were presented: one with a single tether joining the two spacecraft and a novel one where the tether splits into two sub-tethers that are attached to the debris at various locations. This paper provided the planar equations of motion for a TSS and numerically simulated the motion to test the effectiveness of different tether configurations. Experiments were performed at the Spacecraft Robotics and Control Laboratory at Carleton University by tethering two spacecraft together and using air bearings to float them on a flat granite table to create a near friction-free environment, yielding the first published results from this new facility. Experimental results show excellent correlation with the simulated data for the TSS spin scenario, effectively validating the equations of motion presented. Based on the authors' knowledge, these results are also the first published experimental results of detumbling an uncooperative target using

Downloaded by CARLETON UNIVERSITY on January 24, 2017 | http://arc.aiaa.org | DOI: 10.2514/6.2017-1049

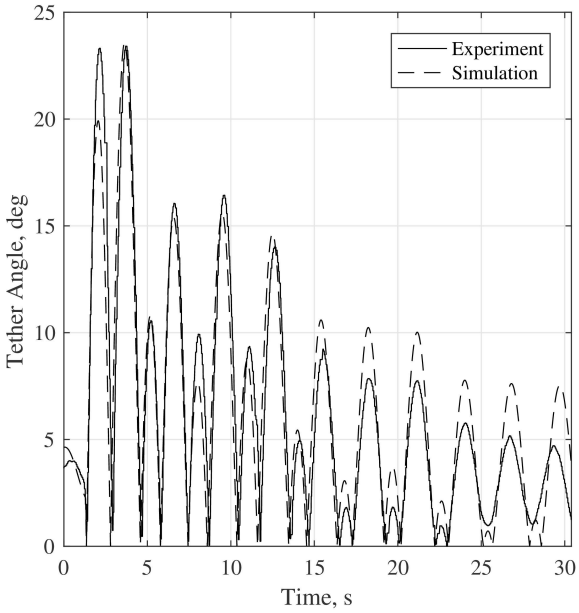

(a) Target tether angle

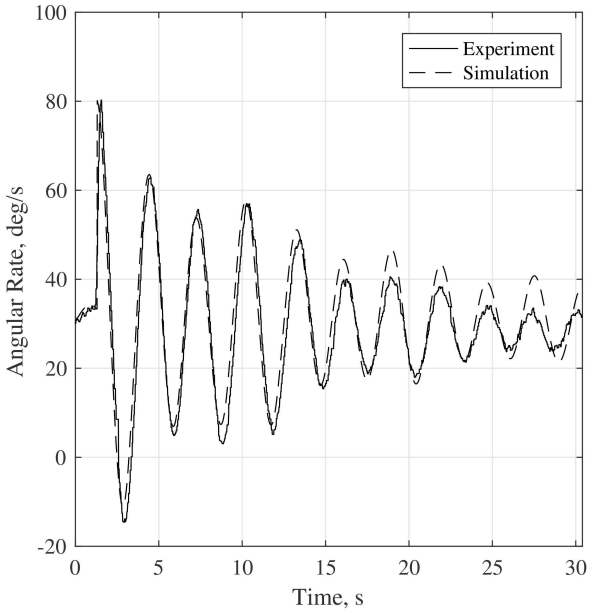

(b) Target angular rate

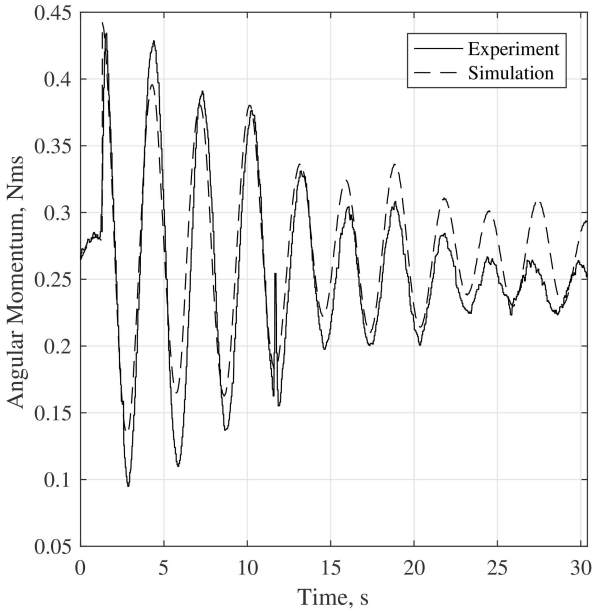

(c) Total angular momentum

Figure 12. Comparing experimental and simulated response for the TSS spin stabilization technique with sub-tethers.

flexible tethers. Small discrepancies are attributed to inaccuracies in tether modeling or other unmodeled effects. The sub-tether configuration significantly outperforms the single tether configuration in its ability to regulate the tether angle, angular rates, and angular momentum of the system for the same initial conditions.

Acknowledgments

This research was financially supported in part by the Natural Sciences and Engineering Research Council of Canada under the Canada Graduate Scholarship CGS M-302098-2015, the Discovery Grant program, and the Ontario Graduate Scholarship.

Downloaded by CARLETON UNIVERSITY on January 24, 2017 | http://arc.aiaa.org | DOI: 10.2514/6.2017-1049

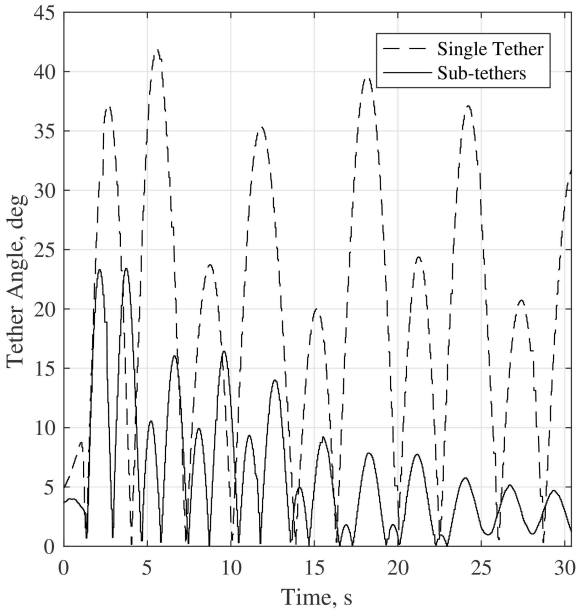

(a) Target tether angle

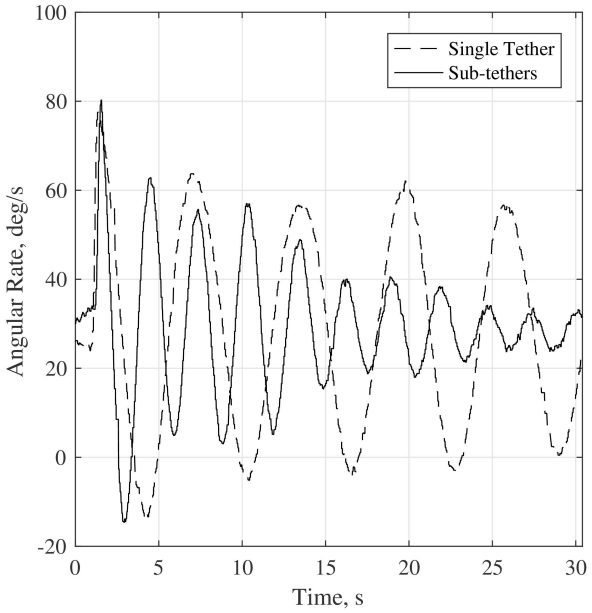

(b) Target angular rate

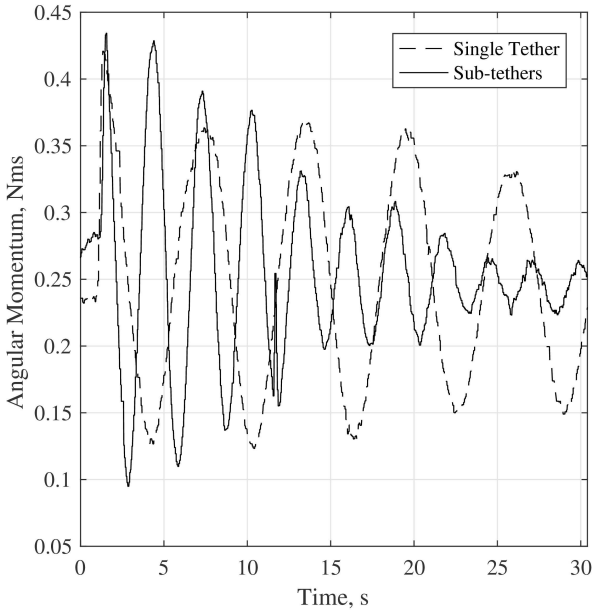

(c) Total angular momentum

Figure 13. Comparing experimental results of the two tether configurations when a TSS spin is used to regulate a tumbling target.

References

[1]Shan, M., Guo, J., and Gill, E., "Review and Comparison of Active Space Debris Capturing and Removal Methods," *Progress in Aerospace Sciences*, Vol. 80, 2015, pp. 18–32.

[2]Kessler, D. J. and Cour-Palais, B. G., "Collision Frequency of Artificial Satellites - The Creation of a Debris Belt," *Journal of Geophysical Research*, Vol. 83, No. A6, 1978, pp. 2637–2646.

[3]Wormnes, K., Le Letty, R., Summerer, L., Krag, H., Schonenborg, R., Dubois-Matra, O., Luraschi, E., Delaval, J., and Cropp, A., "ESA Technologies for Space Debris Remediation," *6th European Conference on Space Debris*, Darmstadt, Germany, 2013.

[4]Kaplan, M. H., Boone, B., Brown, R., Criss, T. B., and Tunstel, E. W., "Engineering Issues for All Major Modes of In Situ Space Debris Debris Capture," *AIAA Space 2010 Conference & Exposition*, Anaheim, CA, 2010.

[5]Persson, S. M. and Sharf, I., "Ground-Based Experiments Towards the Interception of Non-Cooperative Space Debris with a Robotic Manipulator," *IEEE International Conference on Intelligent Robots and Systems*, Hamburg, Germany, 2015.

[6]Reintsema, D., Thaeter, J., Rathke, A., Naumann, W., Rank, P., and Sommer, J., "DEOS - The German Robotics Approach to Secure and De-Orbit Malfunctioned Satellites from Low Earth Orbits," *International Symposium on Artificial Intelligence, Robotics and Automation in Space*, Sapporo, Japan, 2010.

[7]Flores-Abad, A., Wei, Z., Ma, O., and Pham, K. D., "Optimal Control of Space Robots for Capturing a Tumbling Object with Uncertainties," *Journal of Guidance, Control, and Dynamics*, Vol. 37, No. 6, 2014, pp. 2014–2017.

[8]Dudziak, R., Tuttle, S., and Barraclough, S., "Harpoon Technology Development for the Active Removal of Space Debris," *Advances in Space Research*, Vol. 56, No. 3, 2015, pp. 509–527.

[9]Ohkawa, Y., Kawamoto, S., Nishida, S., and Kitamura, S., "Research and Development of Electrodynamic Tethers for Space Debris Mitigation," *Transactions of the Japan Society for Aeronautical and Space Sciences, Space Technology Japan*, Vol. 7, No. ists26, 2009, pp. 5–10.

[10]Iki, K., Kawamoto, S., and Morino, Y., "Experiments and Numerical Simulations of an Electrodynamic Tether Deployment from a Spool-Type Reel Using Thrusters," *Acta Astronautica*, Vol. 94, No. 1, 2014, pp. 318–327.

[11]Johnson, L., Gilchrist, B., Estes, R., and Lorenzini, E., "Overview of Future NASA Tether Applications," *Advances in Space Research*, Vol. 24, No. 8, 1999, pp. 1055–1063.

[12]Botta, E. M., Sharf, I., Misra, A. K., and Teichmann, M., "On the Simulation of Tether-Nets for Space Debris Capture with Vortex Dynamics," *Acta Astronautica*, Vol. 123, 2016, pp. 91–102.

[13]Benvenuto, R. and Lavagna, M., "Flexible Capture Devices for Medium To Large Debris Active Removal: Simulations Results To Drive Experiments," *12th Symposium on Advanced Space Technologies in Automation and Robotics*, Noordwijk, The Netherlands, 2013.

[14]Benvenuto, R. and Lavagna, M., "Net Capturing of Tumbling Space Debris: Contact Modelling Effects on the Evolution of the Disposal Dynamics," *13th Symposium on Advanced Space Technologies in Automation and Robotics*, Noordwijk, The Netherlands, 2015.

[15]Benvenuto, R., Lavagna, M. R., and Salvi, S., "Multibody Dynamics Driving GNC and System Design in Tethered Nets for Active Debris Removal," *Advances in Space Research*, Vol. 58, No. 1, 2016, pp. 45–63.

[16]Medina, A., Cercòs, L., Stefanescu, R., Benvenuto, R., Lavagna, M., Gonzalez, I., Rodriguez, N., and Ormnes, K., "Capturing Nets for Active Debris Removal: A Follow-Up on Microgravity Experiment Design To Validate Flexible Dynamic Models," *13th Symposium on Advanced Space Technologies in Automation and Robotics*, Noordwijk, The Netherlands, 2015.

[17]Cercos, L., Stefanescu, R., Medina, A., Benvenuto, R., Lavagna, M., Gonzalez, I., Rodriguez, N., and Wormnes, K., "Validation of a Net Active Debris Removal Simulator Within Parabolic Flight Experiment," *International Symposium on Artificial Intelligence, Robotics and Automation in Space*, Montreal, Quebec, Canada, 2014.

[18]Lavagna, M., Armellin, R., Bombelli, A., Benvenuto, R., and Carta, R., "Debris Removal Mechanism Based on Tethered Nets," *International Symposium on Artificial Intelligence, Robotics and Automation in Space*, Turin, Italy, 2012.

[19]Linskens, H. T. K. and Mooij, E., "Tether Dynamics Analysis and Guidance and Control Design for Active Space-Debris Removal," *Journal of Guidance, Control, and Dynamics*, Vol. 39, No. 6, 2016, pp. 1232–1243.

[20]Jasper, L. and Schaub, H., "Input Shaped Large Thrust Maneuver with a Tethered Debris Object," *Acta Astronautica*, Vol. 96, 2014, pp. 128–137.

[21]Cleary, S. and O'Connor, W. J., "Control of Space Debris Using an Elastic Tether and Wave-Based Control," *Journal of Guidance, Control, and Dynamics*, Vol. 39, No. 6, 2016, pp. 1392–1406.

[22]Aslanov, V. and Yudintsev, V., "Dynamics of Large Debris Connected to Space Tug by a Tether," *Journal of Guidance, Control, and Dynamics*, Vol. 36, No. 6, 2013, pp. 1654–1660.

[23]Aslanov, V. and Yudintsev, V., "Dynamics of Large Space Debris Removal Using Tethered Space Tug," *Acta Astronautica*, Vol. 91, 2013, pp. 149–156.

[24]Aslanov, V., "Chaos Behavior of Space Debris During Tethered Tow," *Journal of Guidance, Control, and Dynamics*, Vol. 39, No. 10, 2016, pp. 2399–2405.

[25]Hovell, K. and Ulrich, S., "Attitude Stabilization of an Uncooperative Spacecraft in an Orbital Environment using Visco-Elastic Tethers," *AIAA Guidance, Navigation, and Control Conference*, San Diego, CA, 2016.

[26]Hughes, P. C., *Spacecraft Attitude Dynamics*, Dover Publications, Mineola, NY, 2004.

Downloaded by CARLETON UNIVERSITY on January 24, 2017 | http://arc.aiaa.org | DOI: 10.2514/6.2017-1049